CONTRACTING AND ERUPTING COMPONENTS OF SIGMOIDAL ACTIVE REGIONS

RUI LIU[1,2], CHANG LIU[2], TIBOR TÖRÖK[3], YUMING WANG[1], AND HAIMIN WANG[2]
[1] CAS Key Lab of Geospace Environment, Department of Geophysics & Planetary Sciences,
University of Science & Technology of China, Hefei 230026, China; rliu@ustc.edu.cn
[2] Space Weather Research Laboratory, Center for Solar-Terrestrial Research, NJIT, Newark, NJ 07102, USA
[3] Predictive Science Inc., 9990 Mesa Rim Road, Suite 170, San Diego, CA 92121, USA

ABSTRACT

It has recently been noted that solar eruptions can be associated with the contraction of coronal loops that are not involved in magnetic reconnection processes. In this paper, we investigate five coronal eruptions originating from four sigmoidal active regions, using high-cadence, high-resolution narrowband EUV images obtained by the *Solar Dynamic Observatory* (*SDO*). The magnitudes of the flares associated with the eruptions range from *GOES* class B to class X. Owing to the high-sensitivity and broad temperature coverage of the Atmospheric Imaging Assembly (AIA) on board *SDO*, we are able to identify both the contracting and erupting components of the eruptions: the former is observed in cold AIA channels as the contracting coronal loops overlying the elbows of the sigmoid, and the latter is preferentially observed in warm/hot AIA channels as an expanding bubble originating from the center of the sigmoid. The initiation of eruption always precedes the contraction, and in the energetically mild events (B- and C-flares), it also precedes the increase in *GOES* soft X-ray fluxes. In the more energetic events, the eruption is simultaneous with the impulsive phase of the nonthermal hard X-ray emission. These observations confirm that loop contraction is an integrated process in eruptions with partially opened arcades. The consequence of contraction is a new equilibrium with reduced magnetic energy, as the contracting loops never regain their original positions. The contracting process is a direct consequence of flare energy release, as evidenced by the strong correlation of the maximal contracting speed, and strong anti-correlation of the time delay of contraction relative to expansion, with the peak soft X-ray flux. This is also implied by the relationship between contraction and expansion, i.e., their timing and speed.

Key words: Sun: coronal mass ejections (CMEs) – Sun: flares

Online-only material: animation, color figures

1. INTRODUCTION

It is generally regarded that solar eruptions are due to a disruption of the force balance between the upward magnetic pressure force and the downward magnetic tension force. Since the eruption can only derive its energy from the free energy stored in the coronal magnetic field (Forbes 2000), "the coronal field lines must contract in such a way as to reduce the magnetic energy $\int_{\mathcal{V}} B^2/8\pi$" (Hudson 2000, p. L75). The contraction must be associated with the reduction of the magnetic tension force for each individual loop-like field line undergoing contraction, as its footpoints are effectively anchored in the photosphere. Eventually, a new force balance would be achieved between the magnetic pressure and tension force after the energy release. From an alternative viewpoint, the average magnetic pressure $B^2/8\pi$ must decrease over the relevant volume $\mathcal{V}$ across the time duration of the eruption. $\mathcal{V}$ can be roughly regarded as the flaring region, primarily in which magnetic energy is converted into other forms of energies. The contraction process, termed "magnetic implosion" by Hudson (2000), is very similar to the shrinkage of post-flare loops (Forbes & Acton 1996), except that loop shrinkage is driven by temporarily enhanced magnetic tension force at the cusp of the newly reconnected field lines, whereas loop contraction is driven by reduced magnetic pressure in the flaring region. Additionally, with newly reconnected loops piling up above older ones, the post-flare arcade as a whole often expands, rather than shrinks, with time.

Hudson (2000, p. L75) concluded that "a magnetic implosion must occur simultaneously with the energy release," based on

no assumption about the energy release process itself. However, the detailed timing and location of loop contraction might provide diagnostic information on the eruption mechanism. For example, when the reconnection-favorable flux emerges inside a filament channel (Figure 1(a); adapted from Chen & Shibata 2000), it cancels the small magnetic loops below the flux rope, which results in a decrease of the local magnetic pressure. The whole dipolar magnetic structure must contract correspondingly. Meanwhile, plasmas on both sides of the polarity-inversion line (PIL) would move inward to form a current sheet below the flux rope and the subsequent evolution could follow the paradigm of the standard flare model (e.g., Kopp & Pneuman 1976). In that case, overlying coronal loops could be observed to initially contract and then erupt. In a different scenario, a twisted flux rope confined by potential-like magnetic fields is found to be energetically favorable to "rupture" through the overlying arcade via ideal-MHD processes (Figure 1(b); adapted from Sturrock et al. 2001). This is clearly demonstrated in MHD simulations by Gibson & Fan (2006) and Rachmeler et al. (2009), in which overlying loops can be seen to be pushed upward and aside as the flux rope kinks and expands, and after the rope ruptures through the arcade, overlying loops on both sides quickly contract toward the core region, due to the reduction of the magnetic pressure in the core field with the escape of the flux rope. In particular for this scenario (Figure 1(b)), one would expect to see both the expanding flux rope and the contracting overlying loops during the eruption as long as the arcade is only partially opened. Although both scenarios involve a pre-existing flux rope, they can supposedly

Table 1
List of Events

Date	AR	Location	Hale	*GOES*	$v_c^{\max}$ (km s^{-1})[a]	$v_e^{\max}$ (km s^{-1})[b]	Δt (min)[c]
2010 Aug 1	11092	N13E21	α/β	C3.2	−51	83	9.0
2010 Sep 3	11105	N19W23	$\beta/-$	B2.8	−12	94	34.6
2011 Feb 13	11158	S19W03	β/β	M6.6	−195	538	1.8
2011 Feb 15	11158	S21W21	$\beta\gamma/\beta\gamma$	X2.2	−320	401	2.4
2011 Jun 21	11236	N17W19	$\beta\gamma/\beta\gamma$	C7.7	−57	90	12.4

Notes.
[a] Maximum contracting speed.
[b] Maximum expanding speed.
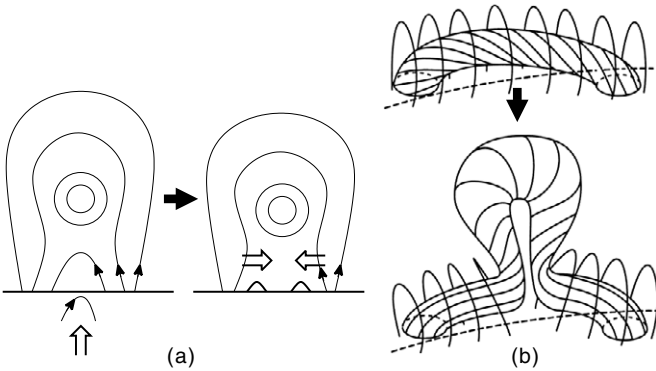[c] Time delay of contraction relative to expansion.

Figure 1. CME models relevant to magnetic implosion. (a) Schematic diagram of the emerging flux triggering mechanism for CMEs (adapted from Chen & Shibata 2000). The emerging flux inside the filament channel cancels the pre-existing loops, which results in the in situ decrease of the magnetic pressure. Magnetized plasmas are driven inward to form a current sheet beneath the flux rope. (b) Schematic sketch showing that in the three-dimensional space a twisted flux rope can rupture the overlying magnetic arcade and erupt by pushing the magnetic arcade aside (adapted from Sturrock et al. 2001). With the escape of the flux rope, the arcade field undergoes contraction due to the decreased magnetic pressure in the core field.

also accommodate those models in which the flux rope forms immediately prior to (e.g., Moore et al. 2001), or during the course of (e.g., Antiochos et al. 1999), the eruption.

Corresponding to the aforementioned models (Figure 1), our previous observational studies also suggest two different scenarios, i.e., (1) the bunch of coronal loops undergoing contraction later becomes the front of the eruptive structure (Liu et al. 2009b) and (2) the contracting loops are distinct from the eruptive structure (Liu & Wang 2009, 2010). The role of contraction in the eruption, however, has been unclear in both scenarios. For Scenario 1, the event reported by Liu et al. (2009b) remains unique in the literature; as for Scenario 2, the eruptive structure is not easy to detect before its appearance as a coronal mass ejection (CME) in the coronagraph, unless there is dense filament material serving as the tracer (Liu & Wang 2009). In some cases, its slow ascension and expansion during the early stage might manifest as the gradual inflation of overlying coronal loops (Liu et al. 2010b). Only with the advent of the *Solar Dynamic Observatory* (*SDO*; Pesnell et al. 2012), which provides a continuous and wide temperature coverage, is the eruptive structure itself more frequently identified beneath the coronagraph height as a hot, diffuse plasmoid (e.g., Liu et al. 2010c; Cheng et al. 2011).

Here in a further investigation of Scenario 2, we identify both the erupting and contracting components using *SDO* data, and hence for the first time we are able to study in detail

their relationship as well as the implication for the eruption mechanism and the associated energy release process. In the rest of this paper, we present in Section 2 the results of our investigation on five flares (Table 1) observed by the Atmospheric Imaging Assembly (AIA; Lemen et al. 2012) on board *SDO*, and we make concluding statements in Section 3.

2. OBSERVATION

2.1. Overview

In addition to the symbiosis of the erupting and contracting components, the five flares studied here all occurred in sigmoidal active regions (Figure 2), which had a sinusoidal shape in the warm AIA channels such as 211 Å (dominated by Fe XIV, $\log T = 6.3$) and 335 Å (dominated by Fe XVII, $\log T = 6.4$) or hot channels like 94 Å (dominated by Fe XVIII, $\log T = 6.8$). Upon close inspection, one can see that two groups of J-shaped loops, which are oppositely oriented with respect to each other, collectively have a sinusoidal appearance (Figure 2). In cold channels such as 171 Å (dominated by Fe IX and Fe X, $\log T = 5.8$) and 193 Å (dominated by Fe XII, $\log T = 6.1$), these regions were dominated by large-scale loops arched over the elbows of the hot sigmoid, suggesting that the highly sheared core field is restrained by the potential-like overlying field. Since nonpotential (sheared or twisted) fields are reservoirs of magnetic free energy, it is not surprising that sigmoidal regions are significantly more likely to be eruptive than non-sigmoidal regions (Hudson et al. 1998; Canfield et al. 1999; Glover et al. 2000), and are deemed to be one of the most important precursor structures for solar eruptions.

Of the five flares, both the M6.6 flare on 2011 February 13 and the X2.2 flare two days later on February 15 occurred in the same AR 11158. One can see that on February 13, when it was still classified as a β-region, AR 11158 was only a "rudimentary" sigmoid compared with its status on February 15. The hot loops in AIA 94 Å in the center of the active region, however, were already highly sheared, taking the similar east–west orientation as the major PIL along which the two bipolar regions interacted and major flares took place (see Beauregard et al. 2012 for details).

Utilizing the newly released vector magnetograms with the 0″.5 pixel size for AR 11158 (Hoeksema et al. 2012) obtained by the Helioseismic and Magnetic Imager (HMI; Scherrer et al. 2012) on board *SDO*, we constructed the non-linear force-free field (NLFFF) model using the "weighted optimization" method (Wiegelmann 2004) after preprocessing the photospheric boundary to best suit the force-free condition (Wiegelmann et al. 2006). NLFFF extrapolation using the vector magnetogram at about 16:00 UT on 2011 February 13
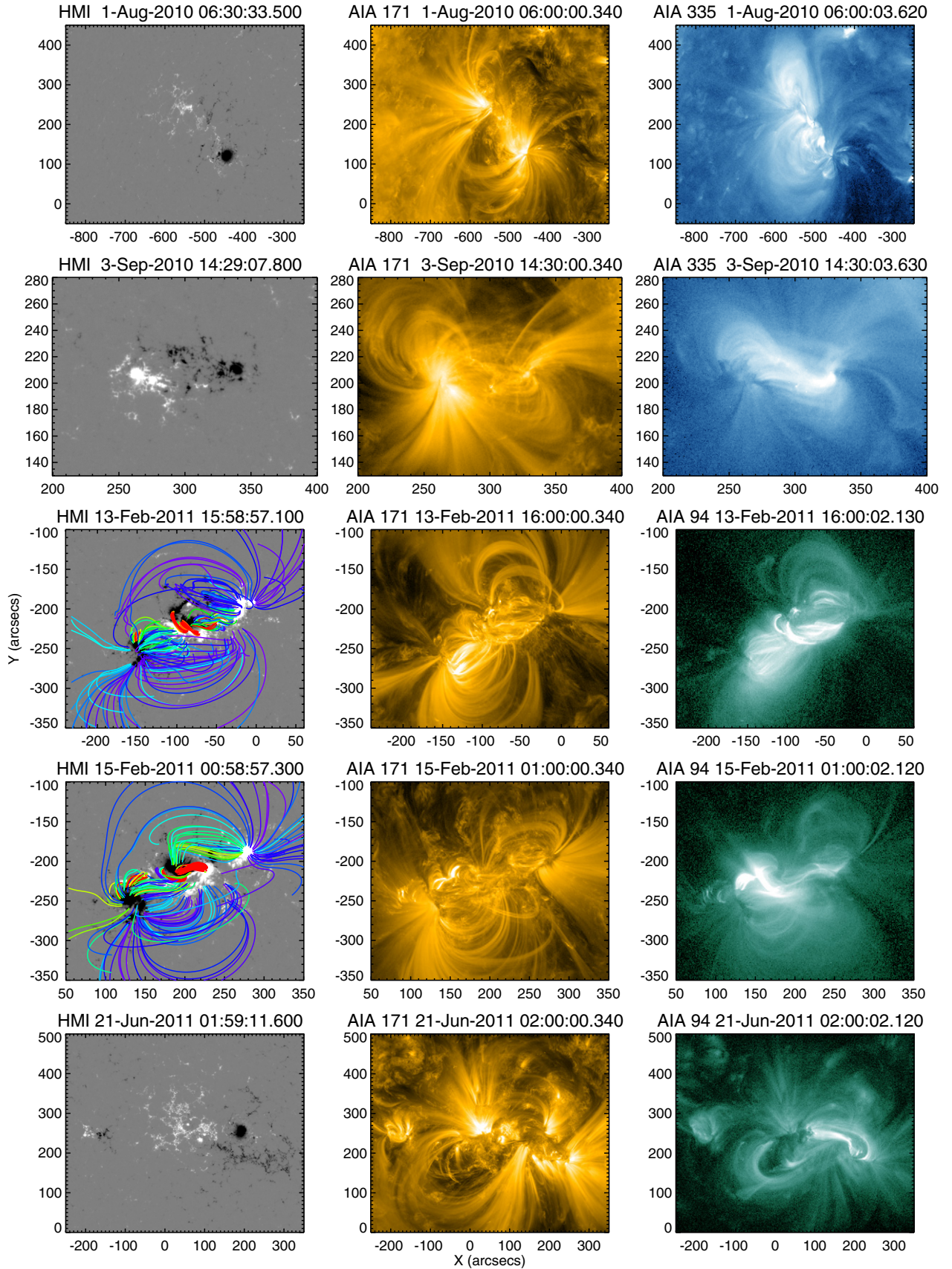
Figure 2. Pre-flare configuration for the five flares studied. Left column: line-of-sight magnetograms obtained by the Helioseismic and Magnetic Imager (HMI) on board *SDO*. Middle and right columns: corresponding EUV images in the cold and warm/hot AIA channels, respectively, showing the sigmoidal morphology and structure. For AR 11158 (third and fourth rows), we use HMI vector magnetograms to construct nonlinear force-free field (NLFFF; see the text for details). The extrapolated field lines are color coded according to the intensity of vertical currents on the surface.

(A color version of this figure is available in the online journal.)
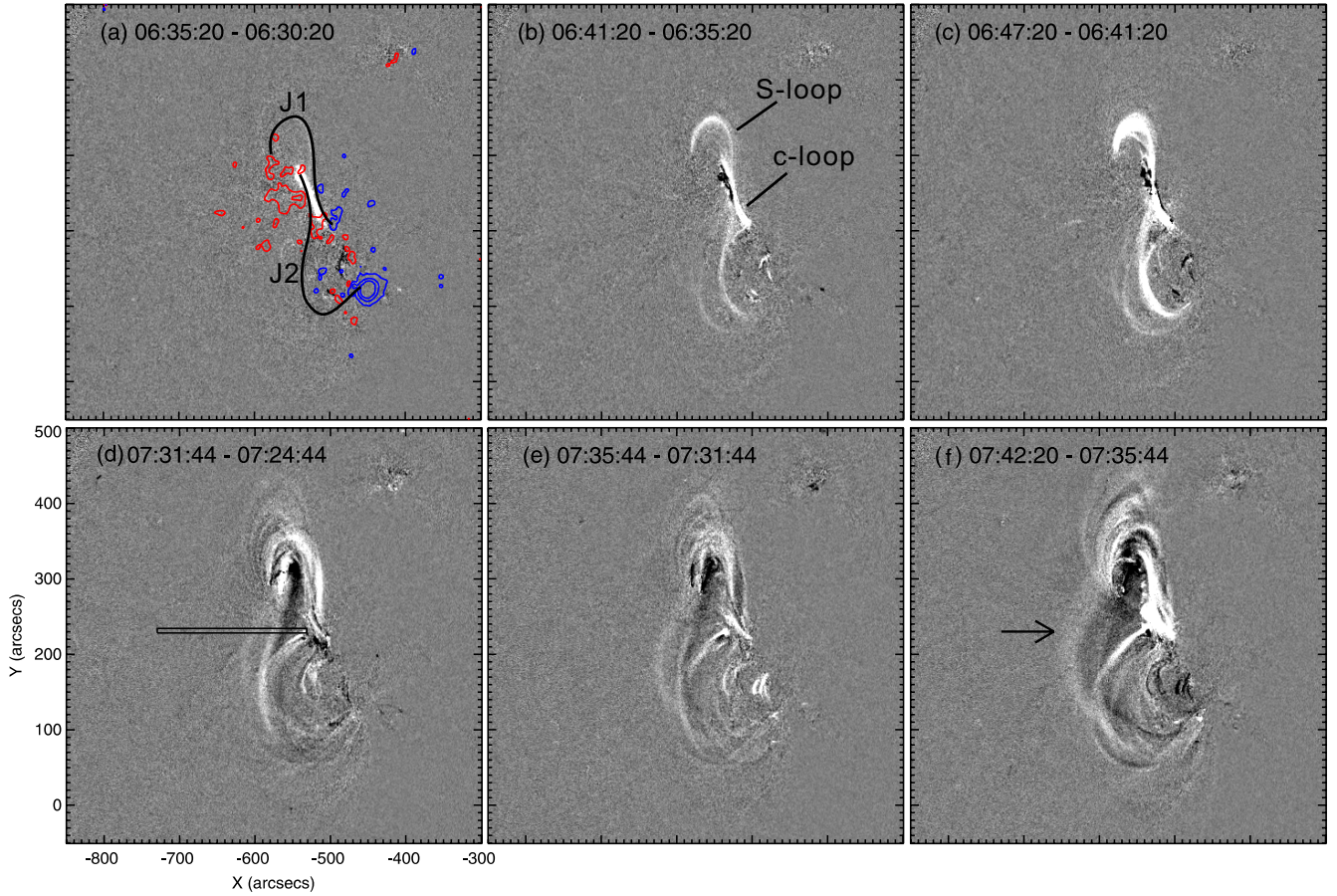
Figure 3. AIA 94 Å difference images, displaying the formation of an S-shaped loop via tether-cutting from two J-shaped loops and its subsequent transformation into a blowing-out bubble marked by an arrow in panel (f). Panel (d) shows the slit through which the space–time diagram in Figure 5(c) is obtained.

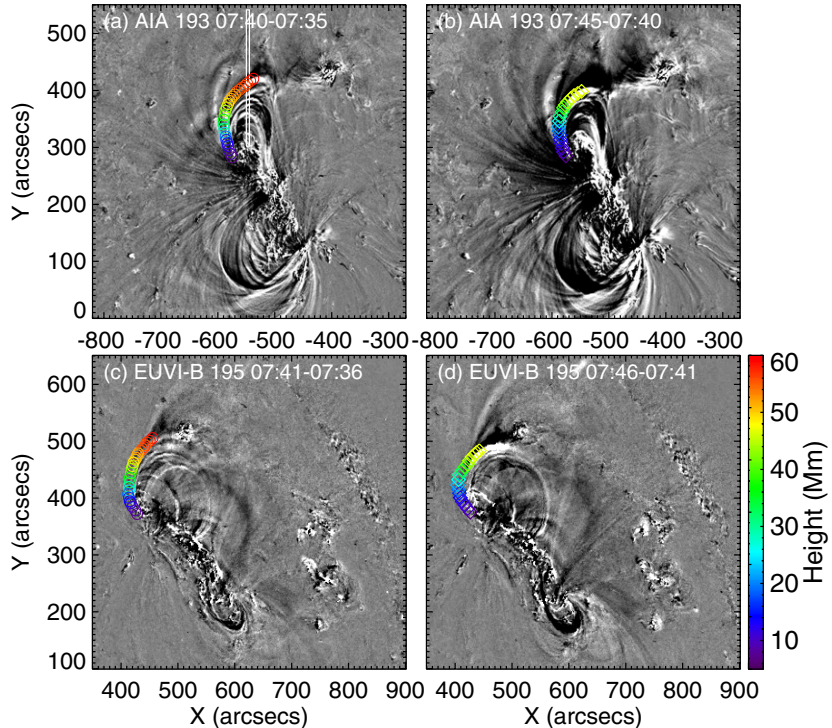(A color version of this figure is available in the online journal.)

Figure 4. Stereoscopic reconstruction of the contracting loop overlying the northern elbow of the sigmoid. The height information of the loop, which is color coded, is obtained by pairing AIA 193 Å and EUVI-B 195 Å images. Panel (a) shows the slit through which the space–time diagram in Figure 5(b) is obtained. The expanding bubble is also visible in both view points, associated with coronal dimming in AIA 193 Å.

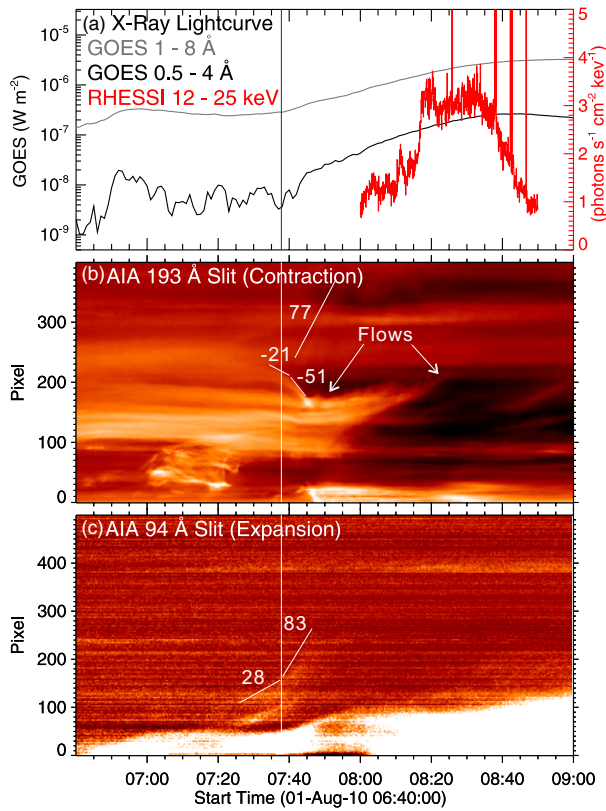(A color version of this figure is available in the online journal.)

Figure 5. Temporal evolution of the contracting loop and the expanding bubble seen through the slits, in relation to the X-ray emission. Numbers indicate speeds of various features in km s^{-1}. The vertical line marks the transition of the exploding bubble from a slow- to a fast-rise phase.

(A color version of this figure is available in the online journal.)

indeed shows highly sheared field lines near the flaring PIL and potential-like field lines overlying it, similar in morphology to the hot and cold coronal loops, respectively (Figure 2). NLFFF extrapolation using the vector magnetogram at about 01:00 UT on February 15 gives a similar result. The extrapolated field lines are color coded according to the intensity of vertical currents on the surface. Field lines whose footpoints are associated with strong current densities (>0.02 A m^{-2}) are in red. The footpoints of these red field lines are cospatial with the four footpoint-like flare brightenings in AIA 94 Å images (Liu et al. 2012; Wang et al. 2012).

2.2. 2010 August 1 Event

The eruption in the sigmoidal region NOAA AR 11093 on 2010 August 1 conformed to the classical "sigmoid-to-arcade" transformation (e.g., Moore et al. 2001), i.e., prior to the eruption, the sigmoidal structure consisted of two opposite bundles of J-shaped loops, and after the eruption, it appeared as a conventional post-flare arcade. The evolution in between the two states was revealed in detail for the first time by AIA observations (Liu et al. 2010c). In the AIA 94 Å difference images (Figure 3), one can see that an S-shaped loop started to glow at about 06:40 UT, about 1 hr before the flare onset. As its glowing was preceded by a heating episode in the core region (Figure 3(a)), the topological reconfiguration resulting in the formation of the continuous S-shaped loop was very likely due to the tether-cutting reconnection (Moore et al. 2001). The S-shaped loop remained in quasi-equilibrium in the lower corona for about 50 minutes, with the central dipped portion rising quasi-statically. During this interval, there was a weak enhancement in *GOES* soft X-rays (SXRs), whose source, however, was located at the southeast limb according
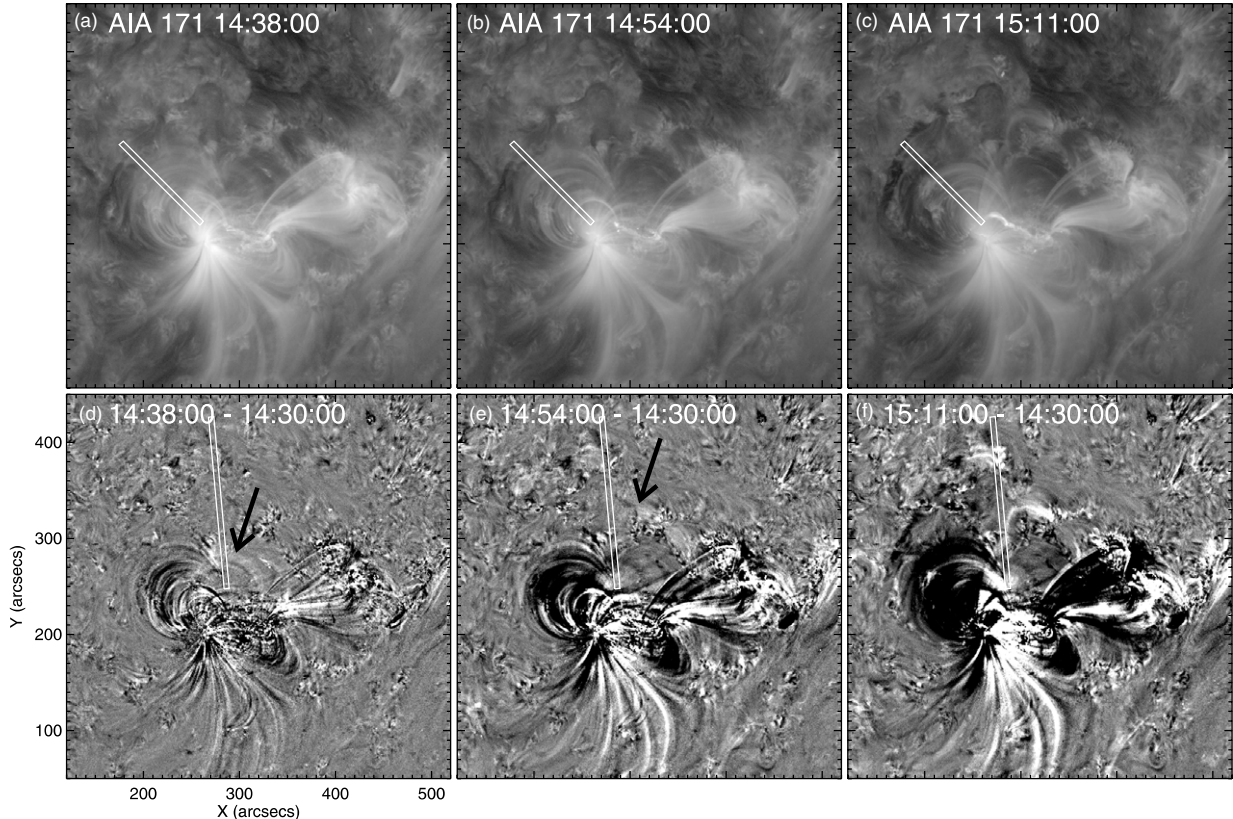

Figure 6. AIA observation of the 2010 September 3 B-flare. Top panels show original 171 Å images and bottom panels show the corresponding difference images. The expanding bubble is indicated by arrows.
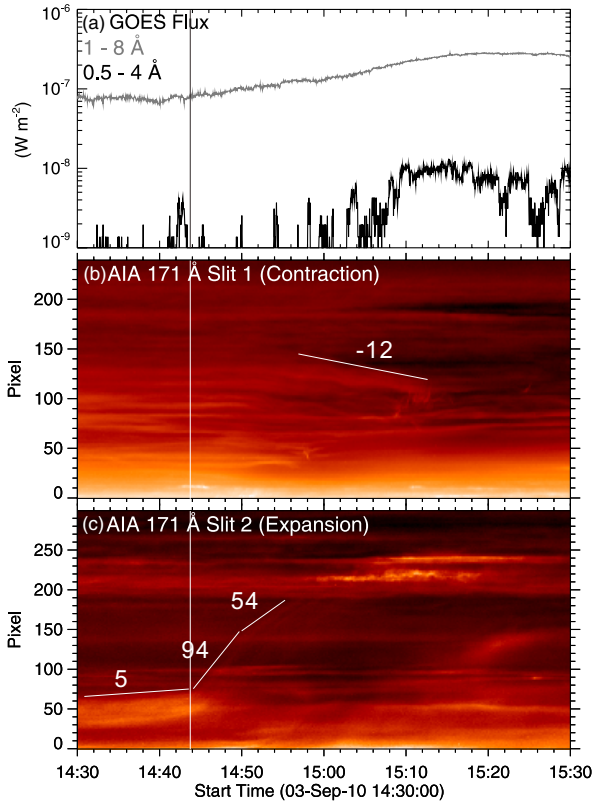
Figure 7. Temporal evolution of the contracting loop and the expanding bubble in relation to the X-ray emission. The space–time diagrams are obtained by stacking image slices cut by the slits shown in Figure 6. The vertical line marks the transition of the exploding bubble from a slow- to a fast-rise phase.

(A color version of this figure is available in the online journal.)

to *RHESSI* observations (see Figure 3 in Liu et al. 2010c). At about 07:30 UT, about 10 minutes prior to the onset of the C3.2 flare, the speed increased to tens of kilometers per second, as the S-shaped loop sped up its transformation into an arch-shaped loop, which eventually led to a CME.

During the eruption, a group of coronal loops overlying the northern elbow of the sigmoid was observed to contract in cold AIA channels such as 171 and 193 Å. The contraction was also visible in EUV images taken by the Extreme-UltraViolet Imager (EUVI; Wuelser et al. 2004) on board the "Behind" satellite of the *Solar Terrestrial Relations Observatory* (*STEREO-B*). The viewing angle was separated by about 70° between *SDO* and *STEREO-B*. By pairing EUVI with AIA images, we are able to derive the three-dimensional location of the loop undergoing contraction via a triangulation technique called *tie point* (Inhester 2006), which is implemented in an SSW routine, SCC_MEASURE, by W. Thompson. From the difference images (Figure 4) one can see both the contracting loop, whose height is color coded, and the expanding bubble, which is associated with coronal dimming in AIA 193 Å. With stereoscopic views, it becomes clear that the contraction is not simply a projection effect due to the loops being pushed aside by the expanding bubble.

We place slits across both the contracting loops (Figure 4(a)) and the expanding bubble (Figure 3(d)). By stacking the resultant image cut over time, we obtain space–time diagrams for a series of AIA 193 and 94 Å images at 12 s cadence (Figures 5(b) and (c)). Note that to increase the signal-to-noise ratio, we integrate over the width of the slit (10 pixels), and that to reveal the diffuse, expanding bubble, we carry out base differencing to make the 94 Å space–time diagram, whereas original 193 Å images are used for the contracting loops which are more clearly
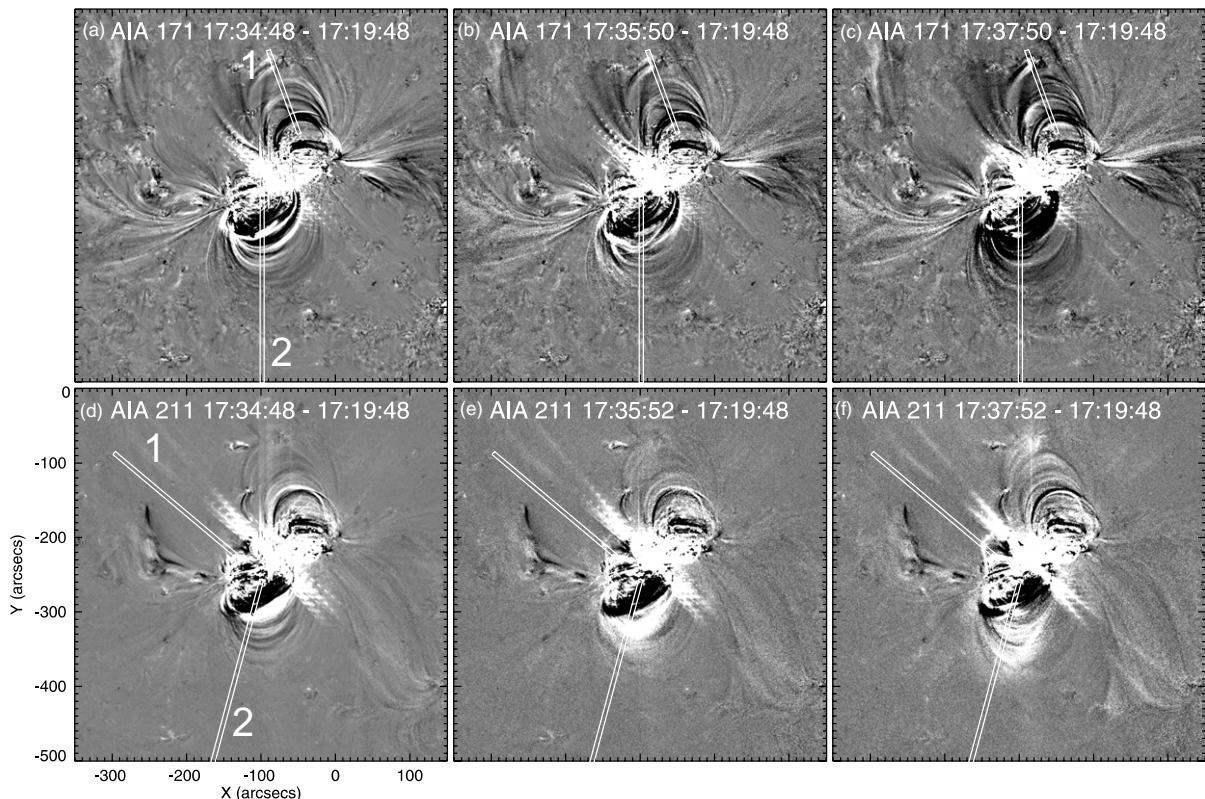

Figure 8. AIA observation of the 2011 February 13 M flare. Top panels show 171 Å difference images and bottom panels 211 Å difference images. An animation of 211 Å images as well as corresponding difference images is available in the online version of the journal.

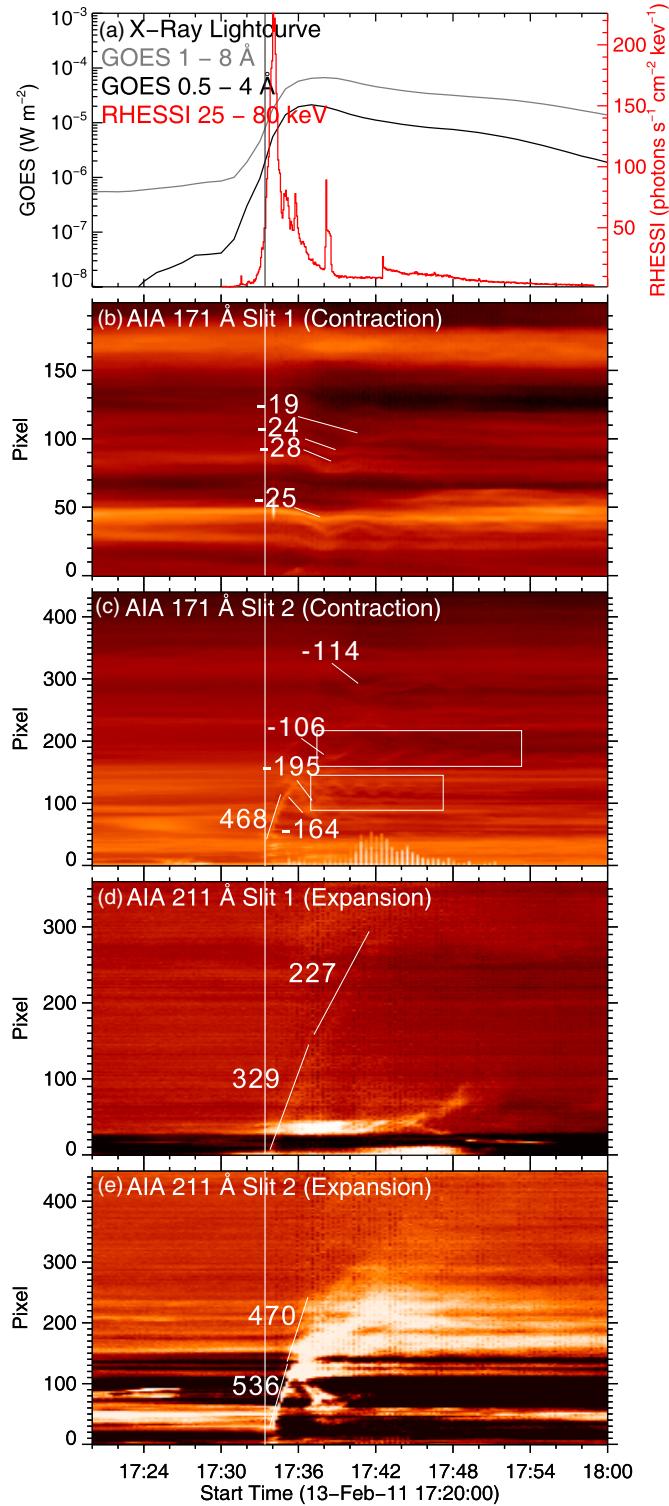(Animation of this figure is available in the online journal.)

Figure 9. Temporal evolution of the contracting loop and the expanding bubble in relation to the X-ray emission. The space–time diagrams are obtained by stacking image slices cut by the slits as shown in Figure 8. The vertical line marks the beginning of the explosion.

(A color version of this figure is available in the online journal.)

The transition time is approximately coincident with the flare onset in terms of the *GOES* 1–8 Å flux. A very diffuse erupting feature can also be marginally seen in the 193 Å space–time diagram, whose speed is similar to the bubble in 94 Å. The contraction of the overlying loops slightly lagged behind the rising of the bubble, and there was a similar transition from slow to fast contraction, slightly lagging behind the speed transition of the bubble by less than three minutes. It is worth noting that the apparently upward-moving feature in the wake of contraction was due to flows along the northern elbow of the sigmoid, not to the recovery of the contracting loops.

2.3. 2010 September 3 Event

In the 2010 September 3 event, both the contracting loops and expanding bubble were visible in the 171 Å channel. But the diffuse bubble can only be seen in the difference images (bottom panels in Figure 6, marked by arrows). The contracting loops were located to the east of the bubble, overlying the eastern elbow of the sigmoid (top panels in Figure 6). Similar to the 2010 August 1 event, in the wake of the bubble erupting, obvious coronal dimming can be seen in the cold AIA channels such as 171 and 193 Å. The dynamics of the bubble can also be characterized by a slow-rise followed by a fast-rise phase, the transition of which coincided with the gradual increase of the *GOES* 1–8 Å flux (Figure 7). The bubble shows a deceleration signature after 14:48 UT. The loop contraction lagged behind the transition time at about 14:44 UT by about 10 minutes.

2.4. 2011 February 13 Event

The 2011 February 13 M6.6 flare was associated with irreversible changes in the photospheric magnetic field (Liu et al. 2012). Using high-resolution and high-precision *Hinode* vector magnetograms and line-of-sight HMI magnetograms, Liu et al. (2012) found that the field change mainly took place in a compact region lying in the center of the sigmoid, where the strength of the horizontal field increased significantly across the time duration of the flare. Moreover, the near-surface field became more stressed and inclined toward the surface while the coronal field became more potential. An intriguing observation is that the current system derived from the extrapolated coronal field above the region with an enhanced horizontal field underwent an apparent downward collapse in the wake of the sigmoid eruption. Liu et al. (2012) concluded that these results are a superimposed effect of both the tether-cutting reconnection producing the flare and the magnetic implosion resulting from the energy release.

Coronal EUV observations agree with the above conclusion drawn from photospheric field measurements regarding magnetic implosion. At the onset of the impulsive phase, two arch-shaped loops originating from the center of the sigmoid were observed to expand outward in 211 Å in different directions (bottom panels of Figure 8) but at similar projected speeds (Figures 9(d) and (e)), while coronal loops overlying both elbows of the sigmoid were observed to contract (top panels of Figure 8), with the loops overlying the eastern elbow contracting much faster (Figures 9(b) and (c)). For this relatively energetic event, the eruption only preceded the contraction by tens of seconds, and the contracting speed becomes as fast as 200 km s^{-1}. In the wake of the contraction, loops overlying the eastern elbow underwent oscillation for several cycles (marked by rectangles in Figure 9), similar to the events studied by Liu & Wang (2010), Gosain (2012), and Kallunki & Pohjolainen (2012). Beyond the
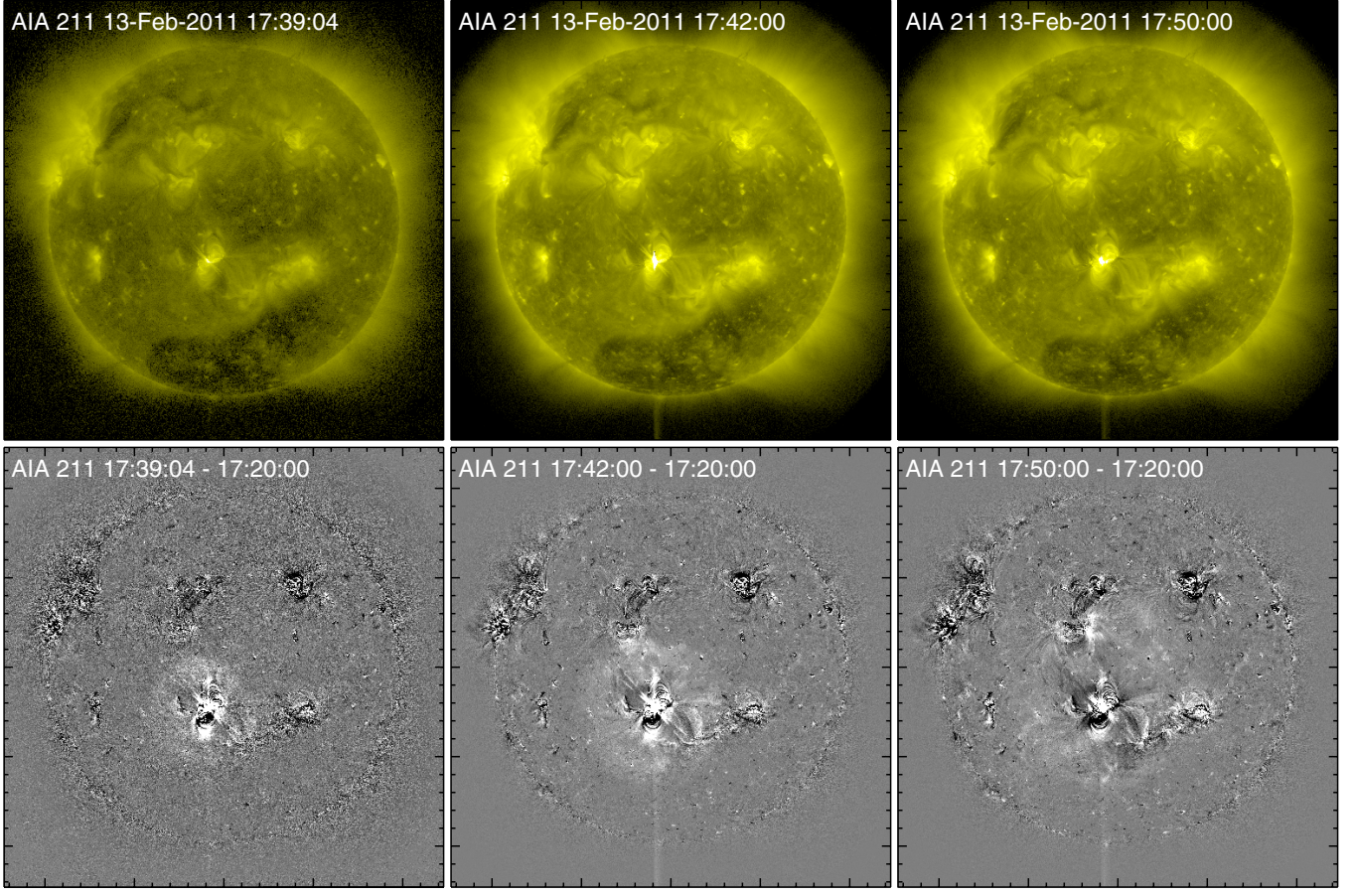
defined in EUV. From Figure 5(c), one can see that the bubble initially rose slowly by ∼30 km s^{-1}, and then transitioned into a phase of fast rise by ∼80 km s^{-1} at about 07:38 UT. The height–time profile is piecewise-linear fitted although the transition is smooth and there seems to be continuous acceleration.

Figure 10. Snapshots of the full-disk AIA 211 Å images (top panels) and the corresponding difference images (bottom panels). In the difference images, a diffuse front can be seen propagating outward from the active region of interest.

(A color version of this figure is available in the online journal.)

expanding loops, one can also see in the animation of the AIA 211 Å difference images (accompanying Figure 8) a diffuse oval front with enhanced intensity propagating outward, well separated from the expanding loops. This oval structure has been identified in MHD simulations as a shell of return currents surrounding the flux rope (Aulanier et al. 2010; Schrijver et al. 2011). From Figure 10 one can see that the front was propagating anisotropically, apparently restrained by nearby active regions and the coronal hole in the southern polar region.

2.5. 2011 February 15 Event

The 2011 February 15 X2.2 flare in AR 11158 is the first X-class flare of the current solar cycle, hence it has generated a lot of interests and has been intensively studied. Kosovichev (2011) reported that the flare produced a powerful "Sunquake" event due to its impact on the photosphere. Wang et al. (2012) reported a rapid, irreversible change of the photospheric magnetic field associated with the flare. Beauregard et al. (2012) studied the shear flows along the PIL as well as the white-light flare emission. Schrijver et al. (2011) investigated the coronal transients associated with the flare. In particular, Schrijver et al. (2011, p. 167) observed "expanding loops from a flux-rope-like structure over the shearing PIL between the central δ-spot groups of AR 11158, developing a propagating coronal front ("EIT wave"), and eventually forming the CME moving into the inner heliosphere." Here the expanding loops are identified as the erupting component.

The active region as seen in the AIA 171 Å channel was dominated by two groups of potential-like loops overlying the elbows of the forward S-shaped sigmoid as seen in the hot AIA channels (Figure 2). Both groups of potential-like loops were observed to contract during the X2.2 flare. In each group, loops underwent contraction successively with those located at lower altitudes starting to contract first, presumably due to the limited propagation speed of the Alfvén wave (see also Liu & Wang 2010; Gosain 2012), whereas loops at higher altitudes had a faster contraction speed (Figures 12(b) and (c)). These contracting/collapsing features were also independently noted by Schrijver et al. (2011), Gosain (2012), and Sun et al. (2012) using different approaches but with similar interpretation, in agreement with Liu & Wang (2009).

Immediately prior to the loop contraction, a bubble (marked by red arcs in the middle panels of Figure 11) can be best seen to originate from the core of the sigmoid and to expand northeastward in the 211 Å channel and southwestward in the 94 Å channel (bottom panels of Figure 11; marked by red arcs). A transition from a slow- to fast-rise phase can still be marginally seen in the 211 Å channel. But the duration of the slow-rise phase was very short, lasting for only about two minutes. The transition time at about 01:50 UT still preceded the loop contraction by about three minutes. The commencement of the bubble expansion at about 01:48 UT was concurrent with the onset of the nonthermal hard X-ray (HXR) emission at 35–100 keV. This expanding bubble was also closely associated with "an expanding intensity front propagating away from the
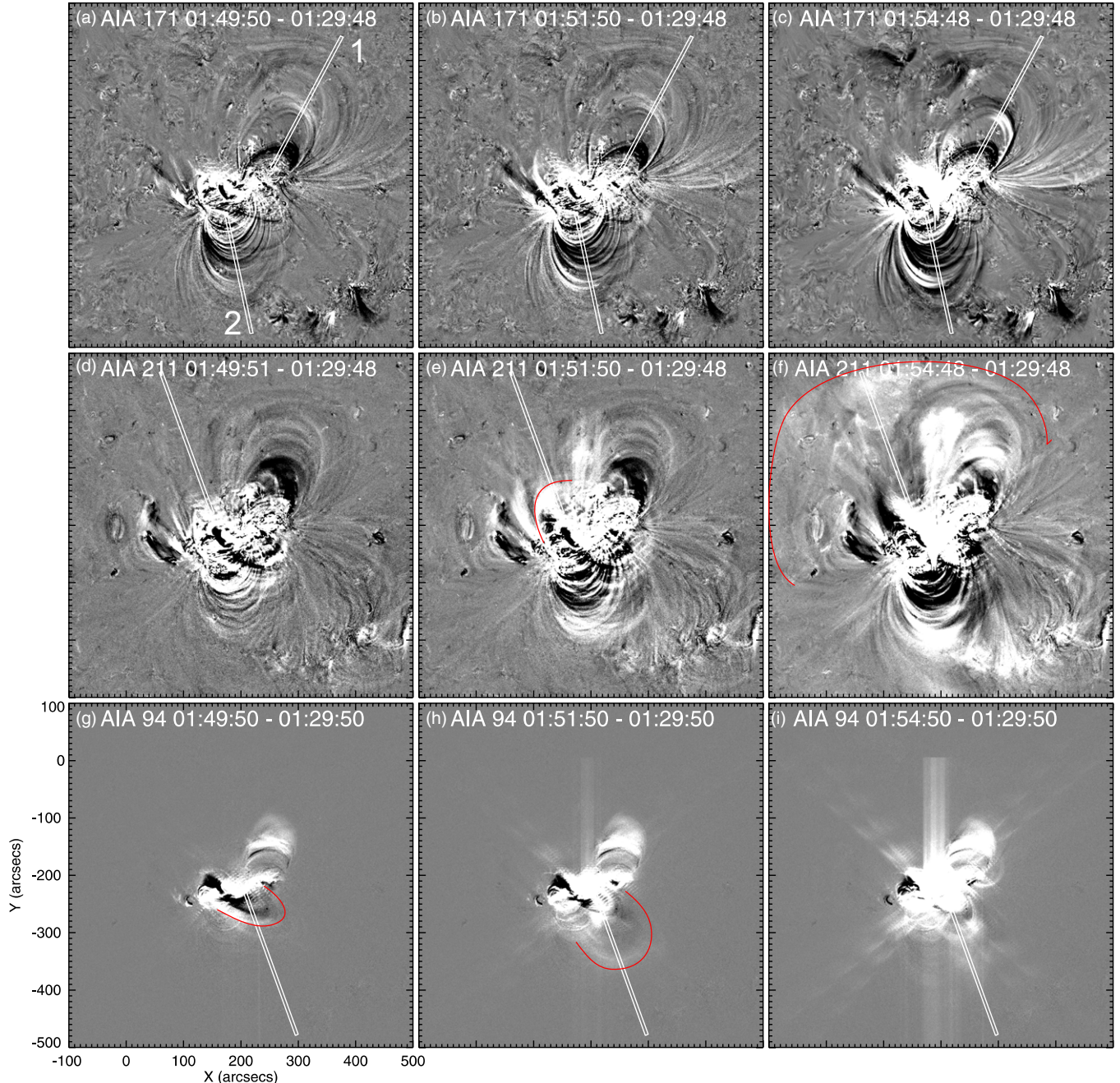
Figure 11. AIA observation of the 2011 February 15 X-flare. From the top, middle, to bottom panels, we show the 171, 211, and 94 difference images, respectively. The expanding bubble is highlighted by red arcs.

(A color version of this figure is available in the online journal.)

flaring region seen on the disk, and the leading edge of the intensity signature of the CME propagating outward from the Sun into the heliosphere," as identified by Schrijver et al. (2011, p. 181). These three distinct features are suggested to be different observational aspects of the eruption of a flux rope (Schrijver et al. 2011). Similar to the February 13 event, in the wake of the contraction, loops overlying both elbows underwent oscillation (see Figure 12, also see Liu & Wang 2010; Gosain 2012; Kallunki & Pohjolainen 2012).

2.6. 2011 June 21 Event

In the 2011 June 21 event, the group of coronal loops overlying the eastern elbow of the sigmoid was observed to

contract in the 171 Å channel (top panels in Figure 13). At the same time, a bubble originating from the center of the sigmoid was observed to expand eastward in the 94 Å channel (bottom panels in Figure 13). Both the contraction and the expansion occurred prior to the C7.7 flare. The transition time of the bubble from a relatively slow- to a fast-rise phase was roughly coincident with the onset of the flare (Figure 14).

3. DISCUSSION AND CONCLUSION

We have investigated four sigmoidal active regions, in which five eruptions with signatures of magnetic implosion occurred. The magnitudes of the flares associated with the eruptions span almost the whole flare "spectrum," from *GOES* class B
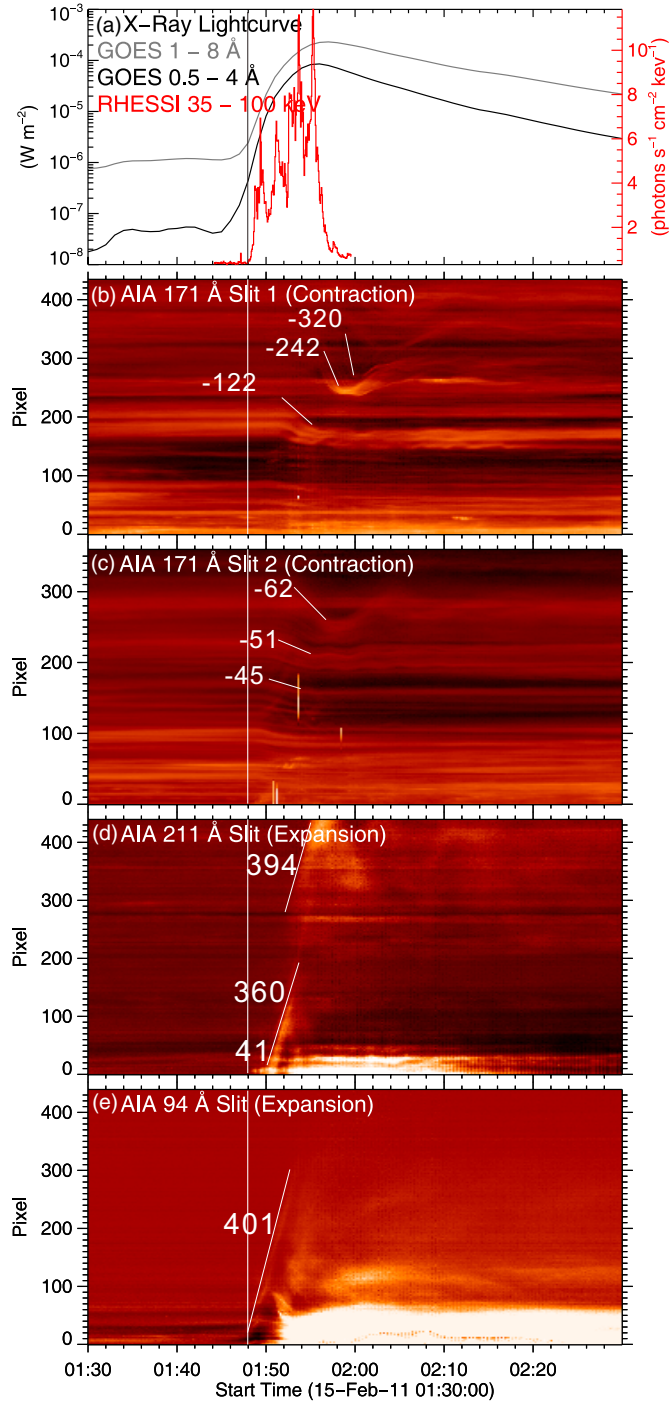
Figure 12. Temporal evolution of the contracting loop and the expanding bubble in relation to the X-ray emission. The space–time diagrams are obtained by stacking image slices cut by the slits as shown in Figure 11. The vertical line marks the beginning of the explosion.

(A color version of this figure is available in the online journal.)

to X. In all of the flares studied, there are both contracting and erupting components: the former is only observed in cold EUV channels and the latter is preferentially visible in warm/hot EUV channels. This is because the contracting component is composed of large-scale, potential-like coronal loops overlying the elbows of the sigmoid, while the erupting component is associated with newly reconnected flux tubes originating from the center of the sigmoid (cf. Liu et al. 2010c; Aulanier et al. 2010; Schrijver et al. 2011). Several important aspects of these observations are discussed as follows.

1. *Consequence of loop contraction.* The overlying loops undergoing contraction never regain their pre-flare positions, which implies a new equilibrium with reduced magnetic energy as the eruption is powered by magnetic energy. One may argue that the apparent contraction of coronal loops could be a projection effect, i.e., the loop plane tilts due to the flare impulse. But in that case, one would expect the restoration of the loops once the flare impulse has passed away. In observations, however, the contracting loops may oscillate about a lower height (e.g., Figure 9; see also Liu & Wang 2010), but never reach the original heights after the eruption. Thus, the contraction within the loop plane must make a significant contribution.

2. *Correlation between contraction and eruption.* The contraction speed seems to depend on the intensity/magnitude of the eruption. From Figure 15, one can see that despite this very small sample size, the peak *GOES* SXR flux as a proxy of the flare magnitude is linearly correlated very well with the measured maximal contraction speed in the log–log plot, although not so well with the maximal erupting speed. Unlike contracting loops which are clearly defined, however, the measurement of the erupting speed involves larger uncertainties as the front of the expanding bubble tends to get more and more diluted and eventually overwhelmed by the background during propagation, thereby leading to underestimation of its speed. One more caveat to keep in mind is that these speeds are not necessarily measured at the time of the peak SXR flux.

3. *Timing.* The eruption precedes the contraction in all of the flares studied, thus establishing loop contraction as a consequence of eruption. There is also a trend that the more energetic the eruption, the smaller the time delay of the loop contraction relative to the onset of the expansion of the erupting component, which is demonstrated in Figure 15 as a strong anti-correlation between the time delay and the peak *GOES* SXR flux in the log–log plot. This time delay is presumably determined by the expansion speed of the erupting component. In addition, in the relatively weak B- and C-flares, the initiation of the erupting component precedes the increase in *GOES* SXR fluxes, but in the stronger M- and X-flares, it is concurrent with the increase in nonthermal HXR fluxes. This may lend support to Lin (2004), who concluded that CMEs are better correlated with flares if there is more free energy available to drive the eruption. However, since the CME progenitor, i.e., the expanding bubble, forms before the flare onset as the weak events clearly demonstrate, the CME must be independent of the conventionally defined flare, or, the flare is only a byproduct of the CME, unless the eruption mechanism for the weak events is different from that for the energetic ones.

4. *Asymmetry of contraction.* The two groups of coronal loops overlying the elbows of the sigmoid often contract asymmetrically, i.e., not only do they contract at different speeds but either group could show little sign of contraction, which depends on the detailed interaction between the core field and the arcade field, including, presumably, their relative strength and the spatial distribution of the decay index of the restraining field (Kliem & Török 2006; Liu et al. 2009a, 2010a). For the 2010 August 1 event in particular, Liu et al. (2010c) concluded that the majority of the flare loops were formed by the reconnection of the stretched legs of the less sheared loops overlying the southern elbow and the center of the sigmoid, based on the reconnection rate
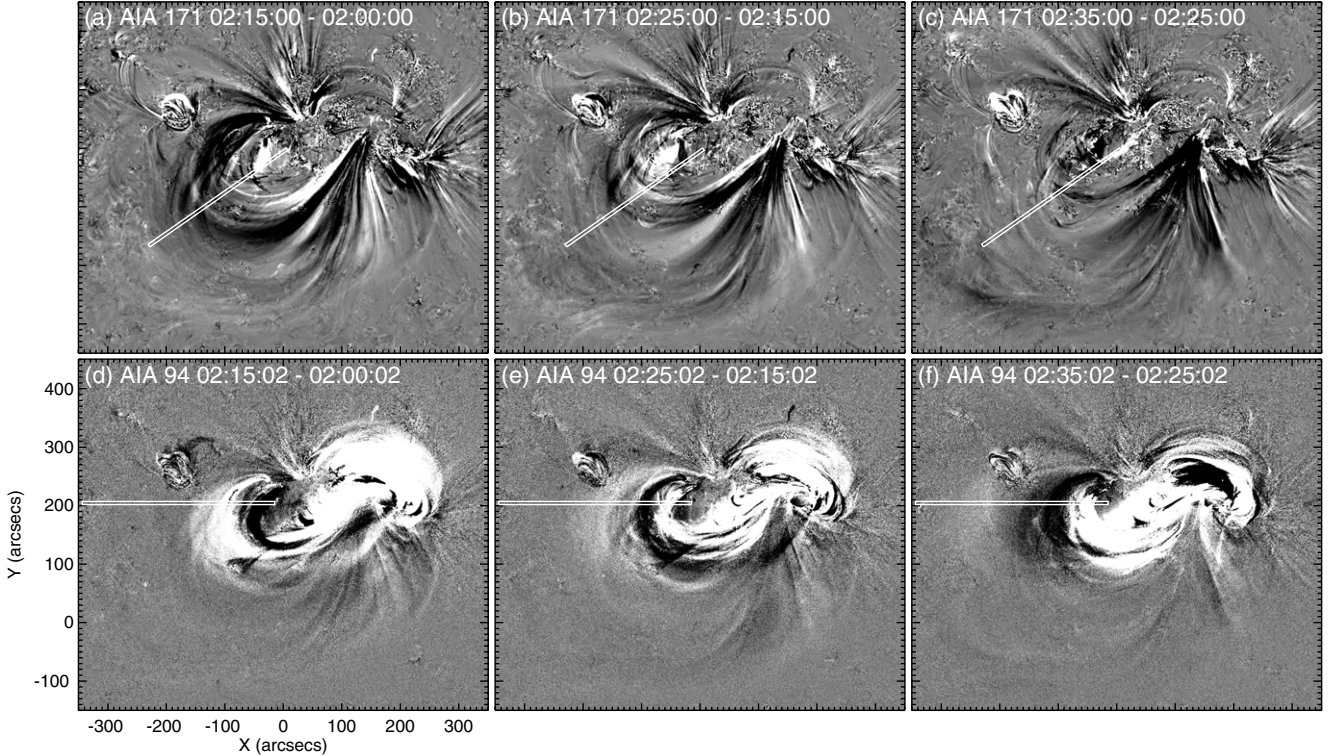
Figure 13. AIA observation of the 2011 June 21 C-flare. The top panels show the 171 Å difference images and the bottom panels the 94 Å difference images.
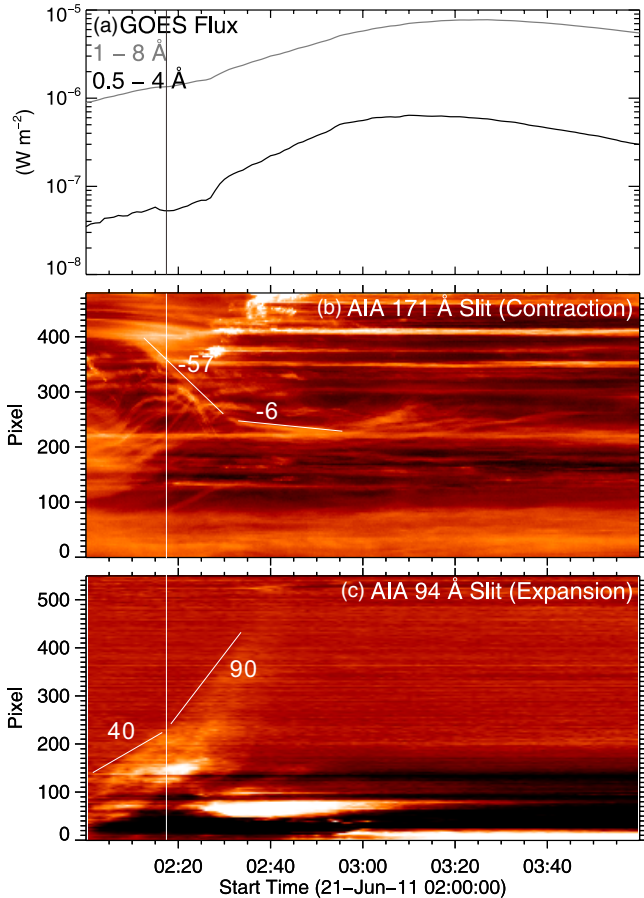

Figure 14. Temporal evolution of the contracting loops and the expanding bubble in relation to the X-ray emission. The space–time diagrams are obtained by stacking image slices cut by the slits as shown in Figure 13. The vertical line marks the transition of the exploding bubble from a slow- to a fast-rise phase.

(A color version of this figure is available in the online journal.)
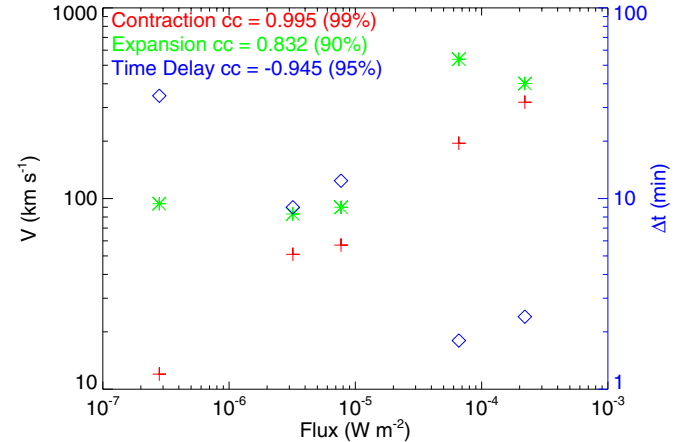
Figure 15. Correlation of the maximal contraction/expansion speed, V, and the time delay of contraction relative to expansion, Δt, with the flare magnitude in terms of the peak *GOES* 1–8 Å flux. The confidence level of the linear correlation coefficient, cc, of $\log(V)$ and $\log \Delta t$ with $\log(F)$ is given in the brackets.

(A color version of this figure is available in the online journal.)

inferred from the Hα ribbon motion. The eruption therefore left most loops overlying the northern elbow unopened. This explains why only these loops underwent obvious contraction. The intensity/magnitude of the eruption could be another relevant factor as among the events studied only those greater than M class show contraction of loops overlying both elbows of the sigmoid.

5. *Implication for eruption mechanism.* As the contracting component is distinct from the erupting component, we conclude that these eruptions conform to the "rupture model" in which the arcade field is partially opened (Sturrock et al. 2001; Figure 1(b)). We can further exclude the breakout model because the coronal loops undergoing

contraction are arched over, rather than located to the side of, the sheared core field. The loop contraction in the latter occasion results from reconnection at the magnetic null above the central lobe in the breakout model.

In conclusion, these observations substantiate that loop contraction is an integrated process in eruptions of sigmoidal active regions in which the restraining arcade field is only partially opened, consistent with theoretical expectations. The consequence of loop contraction is a new equilibrium of the coronal field with reduced magnetic energy, and the process itself is a result of the flare energy release, as evidenced by the strong correlation of the maximal contracting speed, and strong anti-correlation of the time delay of contraction relative to expansion, with the peak SXR flux.

REFERENCES

Antiochos, S. K., DeVore, C. R., & Klimchuk, J. A. 1999, ApJ, 510, 485
Aulanier, G., Török, T., Démoulin, P., & DeLuca, E. E. 2010, ApJ, 708, 314
Beauregard, L., Verma, M., & Denker, C. 2012, Astron. Nachr., 333, 125
Canfield, R. C., Hudson, H. S., & McKenzie, D. E. 1999, Geophys. Res. Lett., 26, 627
Cheng, X., Zhang, J., Liu, Y., & Ding, M. D. 2011, ApJ, 732, L25
Chen, P. F., & Shibata, K. 2000, ApJ, 545, 524
Forbes, T. G. 2000, J. Geophys. Res., 105, 23153
Forbes, T. G., & Acton, L. W. 1996, ApJ, 459, 330
Gibson, S. E., & Fan, Y. 2006, ApJ, 637, L65
Glover, A., Ranns, N. D. R., Harra, L. K., & Culhane, J. L. 2000, Geophys. Res. Lett., 27, 2161
Gosain, S. 2012, ApJ, 749, 85
Hoeksema, et al. 2012, Sol. Phys., to be submitted
Hudson, H. S. 2000, ApJ, 531, L75
Hudson, H. S., Lemen, J. R., St. Cyr, O. C., Sterling, A. C., & Webb, D. F. 1998, Geophys. Res. Lett., 25, 2481
Inhester, B. 2006, arXiv:astro-ph/0612649
Kallunki, J., & Pohjolainen, S. 2012, Sol. Phys., 122
Kliem, B., & Török, T. 2006, Phys. Rev. Lett., 96, 255002
Kopp, R. A., & Pneuman, G. W. 1976, Sol. Phys., 50, 85
Kosovichev, A. G. 2011, ApJ, 734, L15
Lemen, J. R., Title, A. M., Akin, D. J., et al. 2012, Sol. Phys., 275, 17
Lin, J. 2004, Sol. Phys., 219, 169
Liu, C., Deng, N., Liu, R., et al. 2012, ApJ, 745, L4
Liu, C., Lee, J., Jing, J., et al. 2010a, ApJ, 721, L193
Liu, R., Alexander, D., & Gilbert, H. R. 2009a, ApJ, 691, 1079
Liu, R., Liu, C., Park, S.-H., & Wang, H. 2010b, ApJ, 723, 229
Liu, R., Liu, C., Wang, S., Deng, N., & Wang, H. 2010c, ApJ, 725, L84
Liu, R., & Wang, H. 2009, ApJ, 703, L23
Liu, R., & Wang, H. 2010, ApJ, 714, L41
Liu, R., Wang, H., & Alexander, D. 2009b, ApJ, 696, 121
Moore, R. L., Sterling, A. C., Hudson, H. S., & Lemen, J. R. 2001, ApJ, 552, 833
Pesnell, W. D., Thompson, B. J., & Chamberlin, P. C. 2012, Sol. Phys., 275, 3
Rachmeler, L. A., DeForest, C. E., & Kankelborg, C. C. 2009, ApJ, 693, 1431
Scherrer, P. H., Schou, J., Bush, R. I., et al. 2012, Sol. Phys., 275, 207
Schrijver, C. J., Aulanier, G., Title, A. M., Pariat, E., & Delannée, C. 2011, ApJ, 738, 167
Sturrock, P. A., Weber, M., Wheatland, M. S., & Wolfson, R. 2001, ApJ, 548, 492
Sun, X., Hoeksema, J. T., Liu, Y., et al. 2012, ApJ, 748, 77
Wang, S., Liu, C., Liu, R., et al. 2012, ApJ, 745, L17
Wiegelmann, T. 2004, Sol. Phys., 219, 87
Wiegelmann, T., Inhester, B., & Sakurai, T. 2006, Sol. Phys., 233, 215
Wuelser, J.-P., Lemen, J. R., Tarbell, T. D., et al. 2004, Proc. SPIE, 5171, 111